J Mol Model (2007) 13:411–424
DOI 10.1007/s00894-006-0158-3

ORIGINAL PAPER

Dynamic domains and geometrical properties of HIV-1 gp120 during conformational changes induced by CD4 binding

Shu-Qun Liu · Shi-Xi Liu · Yun-Xin Fu

Received: 25 August 2006 / Accepted: 3 October 2006 / Published online: 28 November 2006

Abstract The HIV-1 gp120 exterior envelope glycoprotein undergoes a series of conformational rearrangements while sequentially interacting with the receptor CD4 and co-receptor CCR5 or CXCR4 on the surface of host cells to initiate virus entry. Both the crystal structures of the HIV-1 gp120 core bound by the CD4 and antigen 17b, and the SIV gp120 core pre-bound by the CD4 are known. We have performed dynamic domain studies on the homology models of the CD4-bound and unliganded HIV-1 gp120 with modeled V3 and V4 loops to explore details of conformational changes, hinge axes, and hinge bending regions in the gp120 structures upon CD4 binding. Four dynamic domains were clustered and intricately motional modes for domain pairs were discovered. Together with the detailed comparative analyses of geometrical properties between the unliganded and liganded gp120 models, an induced fit model was proposed to explain events accompanying the CD4 engagement to the gp120, which provided new insight into the dynamics of the molecular induced binding mechanism that complements the molecular dynamics and crystallographic studies.

Keywords HIV-1 gp120 · CD4 · Dynamic domain · Geometrical property · Interaction · Induced fit

Abbreviations

HIV	human immunodeficiency virus
SIV	simian immunodeficiency virus
AIDS	acquired immunodeficiency syndrome
MD	molecular dynamics
Fab	antigen binding fragment
V	variable loop
PND	principle neutralizing determinant
NMR	nuclear magnetic resonance
RMSD	root mean square deviation
CD4-BL	CD4-binding-loop
Rg	radiuses of gyration
SASA	solvent accessible surface area
NNC	number of native contacts
NHB	number of hydrogen bonds
SSE	secondary structure element
CD4BS	CD4-binding site
CD4I	CD4-induced

S.-Q. Liu · Y.-X. Fu (✉)
Laboratory for Conservation and Utilization of Bio-resources,
Yunnan University,
Kunming 650091, People's Republic of China
e-mail: shuqunliu@tsinghua.org.cn

S.-X. Liu
School of Chemical Science and Technology, Yunnan University,
Kunming 650091, People's Republic of China

Y.-X. Fu
Human Genetics Center,
The University of Texas Health Science Center,
Houston, TX 77030, USA

Introduction

During the process of attacking the host immune system, the human immunodeficiency virus HIV-1 and HIV-2 and the related simian immunodeficiency virus (SIV) cause the depletion of $CD4^+$ lymphocytes in their respective hosts, resulting in the development of acquired immunodeficiency syndrome (AIDS) [1, 2]. HIV-1 and SIV's entry into the target cells is mediated by the viral exterior envelope glycoproteins gp120 and gp41, which are organized into trimetric complexes on the viron surface [3–5]. The gp120

undergoes a series of conformational changes when they encounter the receptor CD4 and coreceptor CXCR4 or CCR5 on the surface of a suitable host cell [6–9]. The conformational changes start when CD4 binds to the gp120, which leads to a conformation of gp120 with which a coreceptor can then associate [8–12]. Coreceptor binding induces further conformational changes in the gp120, leading to dissociation of the gp120 from the membrane-anchored gp41. The gp41 then undergoes a series of conformational changes that mediate the fusion process by formation of the fusogenic structure which brings the viral and target cell membranes into close proximity, leading ultimately to the fusion of the viral and target cell membranes [13, 14]. This complex mechanism involves a series of structural rearrangements in the gp120 in which structural dynamics plays a crucial role.

Over the past decades, significant progress has been made toward understanding the interaction between the gp120 and CD4 as well as the HIV-1 entry into the host cell through biochemical, crystallographic, and thermodynamic studies. An important advancement is the determination of the crystallographic structures of the gp120 core in complex with the two amino-terminal domains D1D2 of the CD4 and the antigen binding fragment (Fab) of the human neutralizing antibody 17b [15, 16]. It turns out that the gp120 core is composed of the inner and outer domains and the bridging sheet, which reflects the likely orientation of the gp120 in the assembled trimer. Although the crystal structures of the CD4-bound HIV-1 gp120 core is incomplete due to deletions of residues from both the N- and C-termini; Gly-Ala-Gly tripeptide substitutions for 67 V1/V2 loop residues and 32 V3 loop residues; and no electronic density map for the V4 loop, they nevertheless provide tremendous structural insights for analyzing envelope antigenicity [15–17]. Another advance is the more recent determination of the crystallographic structure of the SIVmac 32H gp120 in a CD4-unliganded conformation that reveals its prefusion state, before interaction with the CD4 [18]. This unliganded SIV gp120 core is also composed of inner and outer domains, and contains neither the variable loops V1/V2 nor the V3, but the V4 loop was resolved. The relatively high overall sequence conservation between SIV and HIV and their shared receptor and coreceptors indicate that the crystal structure of the SIV gp120 does present the conformation in the CD4-unliganded state rather than one of the continuum of flexible conformation selected by the crystallization condition [18]. The rough comparison of structures of the unliganded SIV gp120 and the CD4-bound HIV gp120 revealed that the conformational changes primarily involved the reconfiguration and translocation of structural components in the inner domain and the bridging sheet, while the outer domain was relatively unchanged. The unexpectedly extensive conformational rearrangement upon receptor binding is in agreement with evidence from thermodynamics studies suggesting that the binding of the CD4 or antibodies to the gp120 induces substantial structural rearrangements primarily in the core structure [19, 20]. It has been generally accepted that the gp120-CD4 complex formation leads to the accessibility of the coreceptor binding site. The third variable loop (V3), in particular, plays a central role since it contains not only the principle neutralizing determinant (PND) [21] but also the main coreceptor determinant (CXCR4 and or CCR5 usage) for the HIV-1 at this stage [22]. X-ray crystallographic and nuclear magnetic resonance (NMR) studies of various types of the V3 loop fragments have revealed a high degree of structural heterogeneity [23–26].

Although biochemical studies have described the outline of the fusion process that reveals its vast diversity and sophistication, and crystallographic studies have provided two static snapshots corresponding to the CD4-unliganded and CD4-bound gp120 cores at atomic resolution, respectively, the details of the dynamics at the domain level as well as structural features related to the process of conformational change remain elusive. However, knowledge of the CD4-unliganded and CD4-bound gp120 conformations allows us to better explore issues related to conformational changes induced by the CD4 binding. The purpose of this paper is, on the one hand, to analyze the dynamic domain based on the homology models of unliganded and CD4-bound (liganded) HIV-1 gp120s with modeled V3 and V4 loops to identify domain motional modes, relevant hinge axes, and hinge bending regions, on the other hand, to obtain the detailed changes of the geometrical properties upon gp120 complexation with the CD4, i.e. the changes of solvent accessible surface area (SASA), radiuses of gyration (Rg), number of native contacts (NNC), and secondary structure contents between the two states. Results in this paper led to an induced fit model to explain the binding mechanism of ligands to the gp120.

Materials and methods

Sequence preparation

The initial sequence of the HIV-1 HXBc2 isolate gp160 precursor (Swiss-Prot accession number P04578) was obtained from the Swiss-Prot protein sequence database [27], the sequence of the transmembrane glycoprotein gp41, 52 and 19 residues from the N- and C-termini of the gp120, and the V1/V2 loop (GAG substitutes for 67 V1/V2 loop residues) were subsequently removed. The final gp120 primary sequence consists of residues from 83 to 492, including the sequences of the V3 and V4 loop (Fig. 1).

Template structures preparation

Structural templates of the gp120 core and V3 loop were obtained from PDB protein structure database [28]. PDB entries 1G9M [15] and 2BF1 [18] were used as templates for modeling liganded and unliganded gp120 cores, respectively, and 1CE4 [29] for the V3 loop. For the crystal structure 1G9M, the D1D2 domains of the CD4 (chain C), neutralizing antibody Fab 17b (chains L and H), sugar groups, and crystal water molecules were all removed and only the HIV-1 gp120 core (chain G) was retained. Because the gp120 sequence to be modeled and structural templates 1G9M are both from the HIV-1 HXBc2 strain, their sequence identity is 100%. For the crystal structure 2BF1, sugar groups were removed and only the SIV gp120 core was retained. Since the gp120 core of the SIV and HIV-1 HXBc2 have 35% sequence identity and over 70% sequence similarity, it can serve as an effective template to generate medium-accuracy models of the unliganded HIV-1 gp120 core [30]. The NMR V3 structure (residues 296–331; PDB ID: 1CE4) was manually orientated towards the V3 loop base residues Gly-Ala-Gly of the gp120 core structures from 1G9M (CD4-bound or liganded) and 2BF1 (unliganded) by visual inspection with the VMD program [31], respectively. These two properly orientated V3 loop coordinates were saved as template structures for the V3 loop modeling.

Generation of the liganded and unliganded gp120 models

To obtain homology models of the gp120 with V3 and V4 loops in the CD4-bound conformational state, first, the

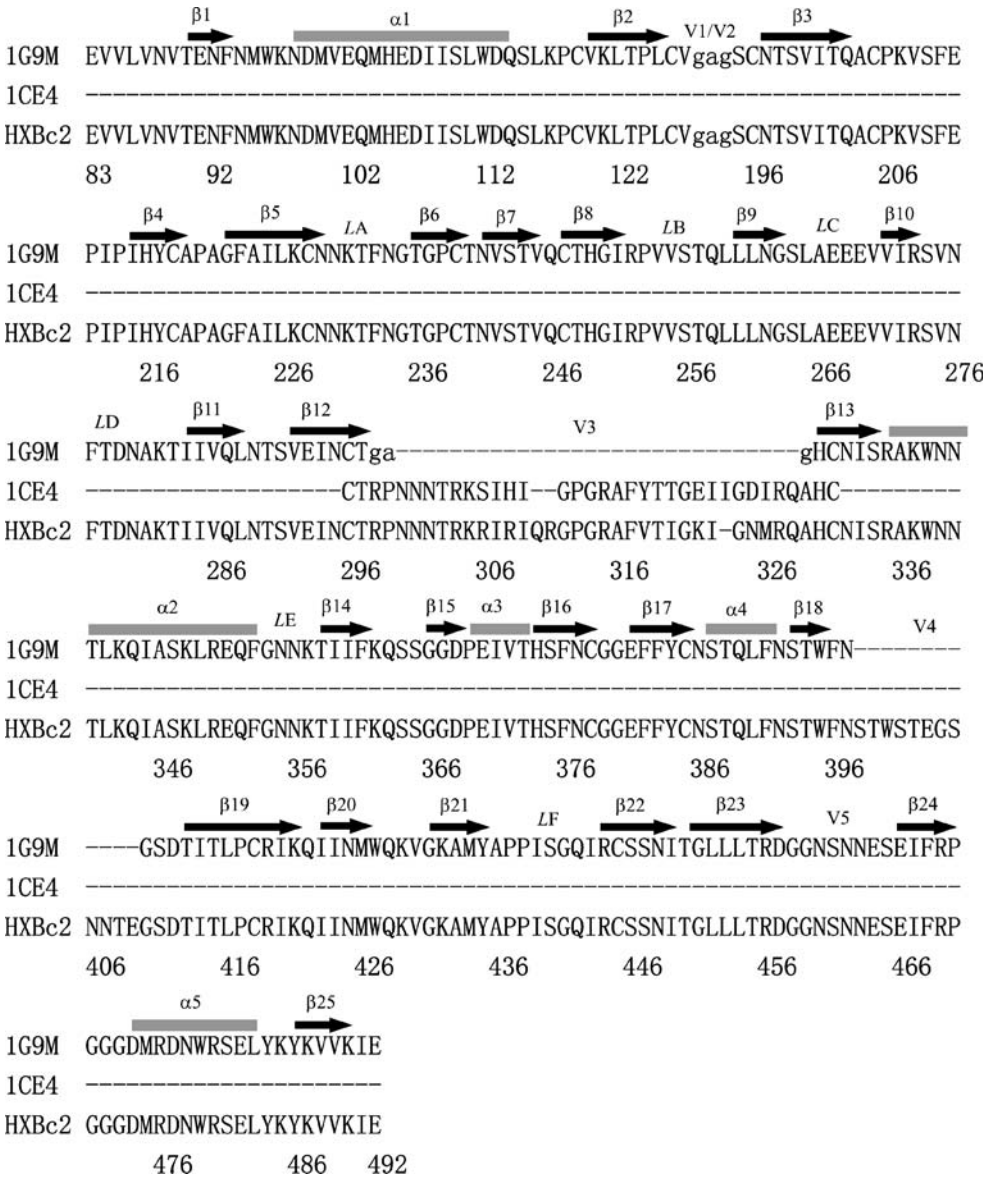

Fig. 1 Multiple sequence alignment between templates of the gp120 core (PDB ID: 1G9M, Chain G) and V3 loop (PDB ID: 1CE4) and the target sequence of the HXBc2 isolate (Swiss-Prot ID P04578). The secondary structure elements are assigned according to X-ray core structure with *arrows* for β-strands and *rods* for α-helices. The "gag" sequence in the V1/V2 and V3 loops of the gp120 core is the consequence of the truncation. The figure was generated by the MODELLER 7v7 program [32]

sequence alignment between the V3 loop (orientated 1CE4), the gp120 core (amended 1G9M) templates and gp120 target sequence was constructed by an in-house written script "alignment" using the MODELLER 7v7 software package [32] (Fig. 1). As shown in Fig. 1, there is a large gap in the V3 loop region between the template sequence of the 1G9M and the target sequence of the HXBc2, while this region is occupied by the template sequence of the V3 loop (1CE4). As expected, another obvious gap occurs in the V4 loop region; Second, 20 gp120 models were generated from the template structures of the gp120 core and the orientated V3 loop using an in-house written script "get-model" for the MODELLER 7v7. The V4 loop coordinates were generated and optimized using a loop modeling sub-routine within the "get-model" with a 3D_INTERPOLATION algorithm and a thorough optimization protocol (a thorough molecular dynamics/simulated annealing procedure and the MD_LEVEL is set to refine_3), respectively; Finally, these 20 models were clustered and an optimized average model was generated by a MODELLER 7v7 script "cluster". The transferred coordinates for a given target atom are the average of the 20 models in the largest cluster of the corresponding atom with the cluster cut off 1.5 Å. The final optimized average gp120 model is in the CD4-bound conformational state, and we referred it to as the liganded (or CD4-bound) gp120 in the rest of the text.

To obtain homology models of the gp120 with V3 loop in its unliganded state, we have to initially obtain models of the unliganded HIV-1 gp120 core from its template, the unliganded SIV gp120 core. The optimized model of the unliganded HIV-1 fsgp120 core and the orientated V3 loop were subsequently used as templates for modeling the unliganded HIV-1 gp120 with the V3 loop. The procedure of sequence alignment, model generation, structure cluster and optimization resembles that of generating the liganded gp120 model. The final optimized average model in the unliganded conformational state was referred to as the unliganded gp120 in the rest of the text.

Dynamic domain analysis

Dynamic domains, hinge axes, and hinge-bending regions in the gp120 were identified and characterized using the DYNDOM program [33, 34]. The basis of the methodology is that the dynamic domains can be distinguished by their differential rotational properties. Given two sets of structures or protein coordinates, DYNDOM assigns rotation vectors for each amino acid residue, which together describe the transition from one conformation to the other. A clustering of the end points of these rotation vectors follows, and if consecutive stretches of residues with similar rotation vectors are found, these are termed dynamic domains. The next stage is the determination of the interdomain screw axis between two dynamic domains. The direction and angle of rotation re this axis represents the vector joining the average points between the two clusters that correspond to the two domains. In the determination of the hinge-bending residues, the rotation of each segment from a domain is projected onto this vector and only the segments at the domain boundaries that are outside one standard deviation from the average of the domain to which they belong, are assigned as bending segments. The unliganded and liganded gp120 models were used as two input coordinates for DYNDOM, and the parameters of window length of residues scanning and minimal domain size were set to different values of combination to obtain reasonable dynamic domains. The parameter for each domain pair connected directly, their ratio of interdomain displacement to intradomain displacement remained at default value 1.0.

Geometrical property analysis

The geometrical properties such as the Rg, NNC and NHB etc. of the unliganded and liganded gp120 models as well as the long, narrow cavity and the CD4-binding cavity in both of the models were calculated using programs g_gyrate, g_mindist, and g_hbond etc. within the GROMACS [35, 36] software package. Secondary structure analyses and SASA calculations were performed with DSSP [37], dihedral angle criteria were taken from PROCHECK [38].

Results

Descriptions of the unliganded and liganded gp120 models

Both of the final optimized homology models of the unliganded and liganded HXBc2 gp120 were composed of 3,471 atoms (include all of the hydrogen atoms), and comprised residues 83–127 and 195–492. A ribbon diagram of the liganded gp120 was shown in Fig. 2a, this model closely resembles its template, the gp120 core from 1G9M [15] with the exception that the liganded model has two additional loops: V3 and V4, and the root mean square deviation (RMSD) between the shared backbone atoms of the model and template is 0.36 Å. All these structural components in the liganded gp120 constitute two major domains, the inner and outer domains, and plus some excursions emanating from the body. The inner domain includes the N- and C-termini, a two-helix, a small two-stranded bundle, a six-stranded β-sandwich at its termini-proximal end and a projection at its distal end from which the V1/V2 stem (β2–β3 ribbon) emanates. The outer

domain is a stacked double barrel that lies alongside the inner domain. The V3 loop connecting the β12 and β13 lies beneath the distal end of the outer domain with the distance between the highly conserved Pro-Gly of the V3 tip and the V3 base about 30 Å. Although certain conformational differences in the V3 loops exist between our gp120 model and the most recently determined crystal structure of a V3-containing gp120 core [26], the extended nature of the V3 in our model is in agreement with the crystal structure. The V4 loop extends away from the right side of the outer domain and adopts an open coiled conformation. The V1/V2 stem and β20–β21 constitute the antiparallel, four-stranded bridging sheet that stands below the distal ends of both the inner and outer domains.

Figure 2b shows the unliganded HIV-1 HXBc2 gp120 model, which resembles its template, the unliganded SIV gp120 core [18], and the RMSD between the common backbone atoms of them is 0.82 Å. The unliganded gp120 model also has two major domains with the inner domain consisting of the N- and C-termini, a three-stranded β-bundle at its termini-proximal end, V1/V2 stem (β2–β3 ribbon), α-helix 1 (α1), and a short α-helix (α5) at the inner/outer domain junction. The unresolved connecting segment (residues 218–228) between the β3 and β4 in the SIV gp120 core corresponds to residues 204–214 in the unliganded HIV-1 gp120, which was generated and optimized using the MODELLER loop modeling subroutine. It presents a disordered conformation that extends away from the V1/V2 stem base of the inner domain. The outer domain has, with some local exceptions, globally the similar structural organization as that in the liganded gp120. The V3 and V4 loops form protruding excursions on the body of the outer domain as they do in the liganded gp120. The major differences between the liganded and unliganded gp120s in the outer domain are: (1) the lengths in loops, for instance, the V4, V5, *L*E are slightly longer in the unliganded form; (2) The connection between strands of the β14 and β16 adopts a extended loop conformation with conserved GGDPE sequence motif in the unliganded gp120, which can be regarded as the "CD4-binding-loop" (CD4-BL) because it moves when CD4 associates and presents a extended strand (β15) and an α-helix (α3) in the CD4-bound conformation, with the β15 forming main-main hydrogen bonding with CD4's C″ strand. The bridging sheet presented in the CD4-liganded gp120 is absent in the unliganded gp120. Although the two β-ribbons, the β2–β3 (V1/V2 stem) and β20–β21 that can form bridging sheet is ordered, a space of 22−29 Å intervenes between them.

In the liganded gp120 model, the receptor CD4 binding sites are composed of the β20–β21 ribbon, V1/V2 stem, loops *L*D, *L*E, V5, β15-α3 excursion, and β24-α5 connection. All of these structural components generate an unusually large CD4 binding cavity (Fig. 2c). The CD4 Phe 43 binding pocket is located at the bottom of the large cavity, specifically, it lies at the intersection of the inner domain, the outer domain, and the bridging sheet, and is deeply buried, extending into the hydrophobic interior of gp120 (Fig. 2c). In the unliganded form, the α1, α5, β20–β21 ribbon, and the CD4-BL create a long, narrow channel at the intersection surfaces of the inner and outer domains (Fig. 2d). Apparently, the binding cavity for the CD4 and binding pocket for the CD4 Phe 43 are absent in the unliganded state.

Domain motions induced by CD4 binding

The dynamic domain analyses were performed on the two forms (unliganded and liganded) of the gp120 models to ascertain the detailed conformational rearrangements at the domain level, as well as whether these domain motions relate to relevant function. The default parameters for the DYNDOM program, the window length 5 and the minimal domain size 20, failure to obtain effective domain motion information because a large part of the gp120 such as the outer domain was not clustered as a domain except that the inner domain was clustered into two subdomains. Therefore, we attempted different combinations of parameter to obtain possible dynamic domains. We found when the arrangement of the window length was seven to eight residues and the domain size was 19–25 residues, the appropriate dynamic domains were able to be clustered using the DYNDOM program based on the structural difference between the liganded and unliganded conformers. Figure 3a shows the motions of four clear quasi-rigid bodies with respect to each other. The outer domain is clustered as an individual dynamic domain (colored yellow in Fig. 3a), whereas the inner domain is clustered into three separately small structural components or subdomains, i.e. the N-, C-terminal subdomain (composed of the N-, C-termini and β5–β7–β25, colored blue in Fig. 3a), the V1/V2 stem (colored red in Fig. 3a), and the α1–β20–β21-part of α5 (colored violet in Fig. 3a). The assignment of residue to these subdomains given above was used to extract the screw axes around which the paired domains rotate with respect to each other. The calculated interdomain screw axes are shown as arrows in Fig. 3. For paired domain motions, the color of the arrow-shaft is identical to that of the fixed domain (the domain whose two conformations are superimposed), while the arrow-head is in the same color as that of the moving or rotating domain. Together, the arrow-head and arrow-shaft describe the direction of rotation of the moving domain relative to the fixed domain by the thumb rule of the right hand, respectively. In the first pair of domains, the N-, C-terminal domain is fixed (2.2 Å backbone RMSD on this domain

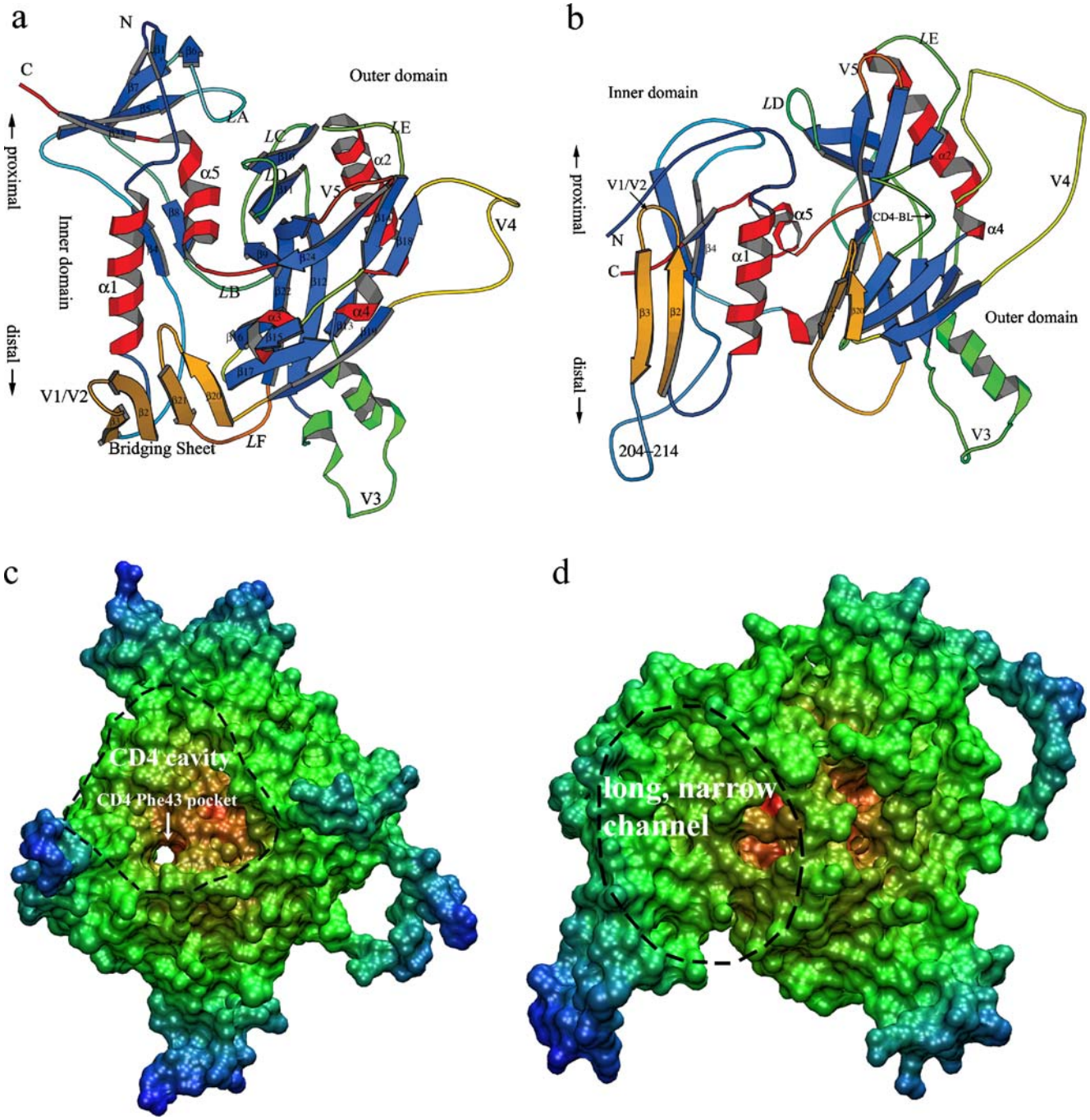

Fig. 2 Structures and molecular surfaces of the gp120 homology models. **a** Ribbon diagram of the liganded gp120, with α-helices in *red*, β-strands in *blue*, bridging sheet in *orange*, and V3 loop in *green*. **b** Ribbon diagram of the unliganded gp120, with the structure elements in the same color as in **a**. **a**, **b** were generated using the MOLSCRIPT program [47]. **c** Solvent accessible surface of the liganded gp120, which is colored according to the accessibility of residues to the solvent, ranging from *blue* (most accessible) to *red* (least accessible). The CD4 binding cavity and CD4 Phe 43 pocket are circumscribed by *black dashes*. **d** Solvent accessible surface of the unliganded gp120, which is *colored* according the principle in **c** and the long, narrow channel is *circumscribed*. **c**, **d** were generated using the VMD program [31]

between the liganded and unliganded models), the moving domain V1/V2 stem rotates around the arrow (arrow-shaft colored blue and arrow-head colored red in Fig. 3a) by very large degrees, 140.9 °, and translates along the screw axis 10.4 Å in the direction prescribed by the arrow-head. The rotating and translational motions of the V1/V2 stem combine to produce a complex set of domain motion relative to the fixed domain, the N-, C-terminal domain. The angle between the rotation axis and the line connecting centers of masses of the two domains is 76.0 °, which means the former is approximately perpendicular to the latter and leads to a closure motion. The details of

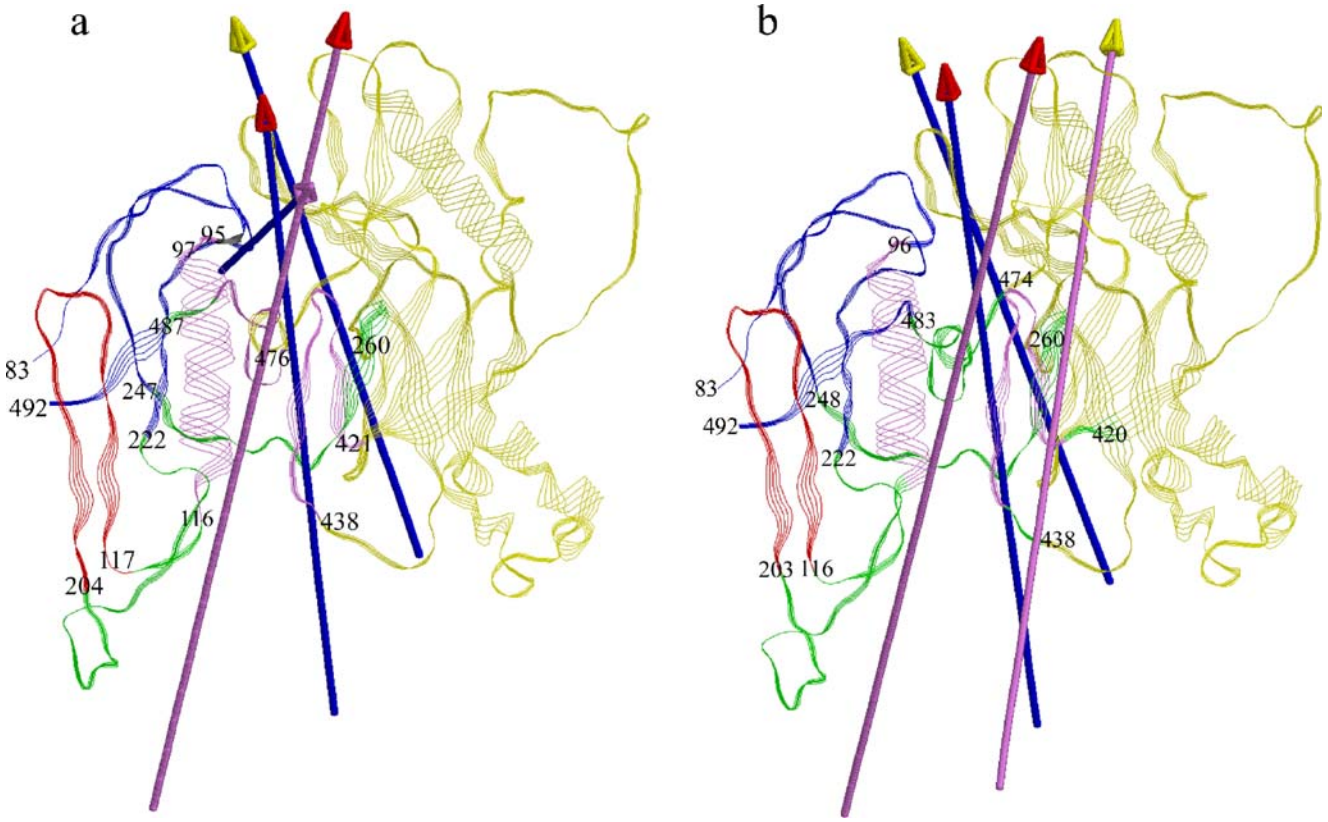

Fig. 3 Dynamic domain analyses of the difference between the unliganded and liganded HIV-1 gp120 homology models. The model for the unliganded gp120 is shown with the *colored arrows* depicting the screw axes for the domain transitions toward the model of the liganded gp120 by the thumb rule of the right hand. The *colors* in the ribbon structures indicate the different clustered domains (*blue*, *red*, *yellow*, *violet*) and the interdomain bending residue regions (*green*). The *colors* in the *arrow-shaft* and *arrow-head* are identical to those of the correspondingly fixed and mobile domains, respectively. The sequence positions of the residue located at the boundaries of the dynamic domains are labeled. **a** DYNDOM result obtained from the combined parameters of window length 7–8 and minimal domain size 19–25. **b** DYNDOM result obtained from the combined parameters of window length 9 and domain size 25. Domain analyses were performed by DYNDOM [34]. Plots were made with RASMOL [48]

quantitative description for paired domain motions are shown in Table 1. The bending residues 204–222 between the two domains constitute a long, flexible linker that is colored green in Fig. 3. Out of the bending residues, residue pairs Pro206-Lys207, Pro212-Ile213, Ala219-Pro220, and Pro220-Ala221 seem to play critical roles as hinge residues because their $\Delta\psi_i+\Delta\varphi_{i+1}$ dihedral angle contribute more than 90% to the total rotation progress of the rotating domain in the direction of the axis. It is worth pointing out that the screw axis represented by the arrow in Fig. 3a is not an "effective hinge axis" because it is about 17.9 Å from the line joining centers of masses of the two domains [34], whereas it is clearly implicated in the domain motion as the main conformation change is seen to occur around this axis.

In the second domain pair, the moving domain (colored yellow in Fig. 3a) that is composed of residues 260–421 and 438–476 from the outer domain and a part of the α5 rotates about 58.2 ° with respect to the fixed domain, the N-, C-terminal domain, and translates 2.4 Å along the screw axis. The screw axis is almost perpendicular to the axis connecting centers of masses of the two domains (82.5 °), resulting in an approximately pure closure motion with percentage of closure extent 98.3% (Table 1). Out of the hinge bending residues 245–260, Cys247-Thr248, Val254-Val255 and Val255-Ser256 are crucial residue pairs to cause domain motion. Being analogous to the first domain pair, the screw axis is not an effective hinge axis in the classical sense because it does not pass near the bending residues.

The third domain pair describes the combined rotation and translation of the moving domain α1–β20–β21-part of the α5 relative to the fixed domain N-, C-termini. The rotation angle and translation distance are 49.7 ° and −0.20 Å, respectively, the latter indicates that the moving domain translates in the opposite direction along the predefined axis. We note that the screw axis in Fig. 3a is approximately parallel to the line joining centers of masses of the two domains, therefore the rotation of the moving domain behaves more like a twisting motion with respect to the N-, C-termini, with merely 29.9% closure motion. There is a short flexible linker consisting of residue 486–487 and the screw axis is not an effective hinge axis for this domain pair.

Table 1 Quantitative results of DYNDOM obtained from the combined parameters of window length 7–8 and minimal domain size 19–25

	Fixed	Residue number	RMSD[d] (Å)	Ratio[e]	Rotation[f] (degrees)	Translation[g] (Å)	Bending residues[h]	Hinge axis[i]	Axis properties[j]	Closure motion[k]
N-, C-termini	Yes	83–95, 222–247, 487–492	2.2							
V1/V2 stem[a]	No	117–204	1.2	7.5	140.9	10.4	204–222	No	76.0/17.9	94.2
Outer domain[a]	No	260–421, 438–476	4.6	1.6	58.2	2.4	245–260	No	82.5/7.1	98.3
α1-β20-β21-α5[a]	No/yes[c]	97–116, 422–437, 477–486	6.3	1.1	49.7	−0.2	486–487	No	33.1/9.7	29.9
V1/V2 stem[b]	No	118–204	1.2	2.4	118.7	11.3	116–118	Yes	50.5/4.8	59.6

[a] The domains move relative to the fixed domain N-, C-termini.
[b] The domain moves relative to α1–β20–β21–α5.
[c] α1–β20–β21–α5 moves relative to the N-, C-termini but is fixed relative to the V1/V2 stem.
[d] Backbone RMSD on this domain between the unliganded and liganded gp120 models
[e] Ratio of interdomain displacement to intradomain displacement
[f] Angle of rotation around the corresponding screw axis
[g] Translation along the screw axis
[h] Hinge bending region between the mobile domain and the fixed domain
[i] The screw axis passing near the bending residue C_α atoms within 4 Å is an effective hinge axis.
[j] Angle/distance between the screw axis and the line joining centers of mass of the two domains
[k] Percentage closure motion

In the fourth domain pair, the fixed domain is composed of the α1, β20–β21 ribbon and a part of the α5, the moving domain is the V1/V2 stem. This pair describes a typical combined motions of rotation and translation, i.e. the V1/V2 stem rotates 118.7 ° and translates 11.3 Å, and in particularly, the angle between the screw axis and the line joining centers of masses of the two domains is 50.5 °, resulting in 59.6% of the closure motion. The final behavior of the motion is a mixed process of closure, twisting, and translation of the V1/V2 stem with respect to the α1–β20–β21-part of the α5. In contrast to the first three domain pairs described above, the screw axis is an effective hinge axis as it passes near the hinge bending region (residues 116–118) with the distance between the axis and the C_α atoms of residue 117 and 118 being 1.7 and 3.9 Å, respectively.

We also found that when we combined other parameters with the window length 9 and the domain size 25 for the DYNDOM we were also able to obtain proper dynamic domain pairs. Fig. 3b shows the qualitative description of domain motions with respect to each other, the detailed quantitative descriptions of rotation angle, translation distance, bending residue, motion behavior, and hinges axis are shown in Table 2. Similar to the results from the first combined parameters, four domain pairs were clustered. They are the N-, C-termini vs V1/V2 stem, N-, C-termini vs outer domain, α1–β20–β21 vs V1/V2 stem, and α1–β20–β21 vs the outer domain, with the first domain in each domain pair being the fixed domain. The differences between the results obtained from the two sets of parameters are the residue quantity assigned to the individual domain and the variable pairing combination of domains. For instance, the α1–β20–β21 domain colored violet in Fig. 3b does not include the fraction of the α5 (residues 477–486) while the result obtained from the first combined parameters does (Fig. 3a and Table 1). The α5 segment is assigned to the hinge bending region between the N-, C-termini and outer domains, which seems to be more reasonable than when the α5 is separately assigned to the outer domain and α1–β20–β21 domain because the α5 resides at the junction of the inner and outer domains. We also noted that the screw axis of the N-, C-termini vs outer domain became an effective hinge axis as it passed near their hinge bending region, the α5. The second combined parameters did not obtain the twisting motion of the α1–β20–β21–α5 with respect to the N-, C-termini, but obtained an additional domain pair, α1–β20–β21 vs outer domain, which describes a mixed motions of rotation (49.8 °) and translation (1.2 Å) of the outer domain relative to the α1–β20–β21. This domain pair has effective hinge axis with 62.0% closure motion, indicating the partial twisting mode occurs in the process.

Geometrical property analyses

The unliganded and liganded gp120 models were subject to a number of structural analyses to assess conformational differences between them at the quantitative level (Table 3). The quantities for networks of hydrogen bond and native contact with inter-atomic distance less than 6 Å are both larger in the liganded state than in the unliganded state, resulting in more secondary structure contents in the liganded form. Despite few differences in the radiuses of gyration (Rg) of both the conformational states, the total (hydrophobic plus hydrophilic) solvent accessible surface area (SASA) of the liganded state is 4,065.1 $Å^2$ smaller than that of the unliganded state. All of the geometrical properties calculated from the two gp120 models indicate that the liganded gp120 adopts a more compact and ordered

Table 2 Quantitative results of DYNDOM obtained from the combined parameters of window length 9 and minimal domain size 25

	Fixed[c]	Residue number	RMSD[d] (Å)	Ratio[e]	Rotation[f] (degrees)	Translation[g] (Å)	Bending residues[h]	Hinge axis[i]	Axis properties[j]	% Closure motion[k]
N-,C-termini	Yes	83–96, 222–248, 483–492	2.8							
V1/V2 stem[a]	No	116–203	1.5	5.6	138.4	10.3	203–222	No	76.4/17.3	94.5
Outer domain[a]	No	260–420, 438–474	4.6	1.4	58.4	2.1	244–260, 475–483	Yes	82.0/6.7	98.0
α1-β20-β21	Yes	97–115, 421–437	4.9							
V1/V2 stem[b]	No	116–203	1.5	2.6	119.4	11.8	114–116	Yes	49.2/2.0	57.4
Outer domain[b]	No	260–420, 438–475	4.6	1.1	49.8	1.2	420–421, 437–438	Yes	51.9/2.5	62.0

[a] The domains move relative to the fixed domain N-, C-termini.
[b] The domains move relative to the domain α1–β20–β21.
[c] Whether the domain is fixed or mobile
[d] Backbone RMSD on this domain between the unliganded and liganded gp120 models
[e] Ratio of interdomain displacement to intradomain displacement
[f] Angle of rotation around the corresponding screw axis
[g] Translation along the screw axis
[h] Hinge bending region between the mobile domain and fixed domain
[i] The screw axis passing near the bending residue C_α atoms within 4 Å is an effective hinge axis.
[j] Angle/distance between the screw axis and the line joining centers of mass
[k] Percentage closure motion

conformation than the unliganded one. The large RMSD (10.5 Å) of the shared backbone of the two models primarily stems from the reposition of the structural components in the inner domain as can be readily seen by overlapping the liganded gp120 against the unliganded one with linear frames interpolating between them (Fig. 4). It is worth pointing out that the interpolated frames between them do not represent the conformational transition pathway but merely highlight the primary structural differences. The dramatically structural rearrangements within the inner domain are in line with the dynamic domain analyses described above, where the majority of the moving subdomains (such as V1/V2 stem and α1) primarily arise from the inner domain. Especially for the V1/V2 stems of the inner domain, although their intradomain backbone RMSDs possess the lowest values (usually less than 1.5 Å, see Tables 1 and 2) among these subdomains, their ratios of interdomain displacement to intradomain displacement possess the largest values (usually more than 2.4, see Tables 1 and 2), indicating the V1/V2 stem undergoes the most dramatically conformational reorientation upon the CD4 binding, and this is also reflected by its largest rotation and translation. On the contrary, although intradomain RMSDs of the outer domain (4.6 Å) are larger than those of the V1/V2 stem, the lower ratios (less than 1.6) of the interdomain displacement to intradomain displacement indicate that the entire outer domain undergoes relatively moderate conformation reorientation compared to the subdomains in the inner domain. However, Fig. 4 illustrates that individual components such as the β20–β21 ribbon, CD4-BL, *L*D, *L*E, *L*F, as well as the V3, V4, and V5 loops in the outer domain undergo large conformational rearrangements. In particular, the β2–β3 and

Table 3 Geometrical properties of the unliganded and liganded gp120 models

	RMSD[b] (Å)	NHB[c]	SASA[d] (Å^2)	NNC[e]	Rg[f] (Å)	DIH[g]	ENE[h] (kJ/mol)	SSE[i]		
								α helix	β sheet	Turn
Unliganded[a]	0.0	160.0	23,735.4	15,6282.0	22.09	10	−33,956.5	60	41	13
Liganded[a]	10.5	208.0	19,670.3	163,758.0	22.13	6	−34,311.1	118	57	21

[a] Geometrical properties of the unliganded and liganded gp120 models, respectively
[b] Backbone RMSD with respect to the unliganded gp120 model
[c] Number of hydrogen bonds. A hydrogen bond is considered to exist when the donor-hydrogen-acceptor is larger than 120 ° and the donor-acceptor distance is smaller than 3.5 Å.
[d] Total solvent accessible surface
[e] Number of native contacts. A native contact is considered to exist if the distance between the two atoms is less than 6 Å.
[f] Radius of gyration
[g] Number of residues in the disallowed regions in the Ramachandran plot [46].
[h] Potential energy after energy minimization in the GROMOS96 force field.
[i] Number of residues in the corresponding secondary structure elements.

β20–β21 hairpins' mutual approach in space, together with the α1's excursion, results in the two halves of the bridging sheet closing up over the α1 and subsequently the final formation of the integrated bridging-sheet.

We have also calculated the SASA difference per residue for both the conformational states to examine the pattern of solvent exposure in different regions of the protein. Figure 5 shows that a large proportion of the conformational segments in the liganded state have the decreased SASA compared to the unliganded one. In particular, the regions with residues 203–275 composed of the β3–β4 linker and β4 to β9; the regions with residues 330–395 composed of the β13, α2, β14, CD4-BL (or β15–α3 in the liganded state), β16 to β18, and α4; and residues 413-484 composed of the β19 to β24 and α5, have the decreased SASA in the liganded state as a whole, despite bits of residues with the increased SASA interspersed between them. However, more than 65% residues in the β2–β3 ribbon (V1/V2 stem), V3, V4 and V5 loops increase their SASA in the liganded gp120. The residues with decreased SASA in the V1/V2 stem, loop *L*D, CD4-BL, V5, β20–β21 linker, and β24–α5 linker may contribute to the formation of the CD4 binding cavity, while the residues with increased SASA in these structural components may be responsible for the interaction with CD4, especially for the β2–β3 ribbon (V1/V2 stem), its increased SASA might also be of great benefit to the association of the coreceptor or CD4i antibodies.

As described above, the α1, α5, β20–β21, and CD4-BL in the unliganded state create the long, narrow channel that has been identified to be the initial contact sites for the CD4, CD4BS antibodies and small molecules inhibiting the HIV-1 entry [18]. On the contrary, the *L*D, V5, β15–α3, β20–β21 linker and β24–α5 linker in the liganded form constitute the CD4 binding cavity [15]. We therefore calculated the RMSD, number of hydrogen bond (NHB), total SASA, Rg, and number of native contact (NNC) of the residues forming the two cavities within the unliganded and liganded states, respectively (Table 4). The variations of the Rg, SASA, NNC and HNB for the two states are correlated, i.e. an increase in the Rg corresponds to an increase in the SASA and decreases in the NNC and NHB, and vice versa. Concretely, the long, narrow cavity in the unliganded state has a larger Rg and more SASA whereas fewer NNC and NHB than in the liganded state. On the contrary, the CD4 binding cavity in the unliganded state has a smaller Rg and fewer SASA while more NNC and NHB than in the liganded. For both the cavities in the same conformational state, the SASA, NNC and NHB of the long, narrow cavity are larger than those of the CD4 binding cavity because the former consists of more residues than the latter. As thus, these analyses point out the structural changes for the CD4 access channel, together with the large RMSDs of the two cavities in the liganded state relative to the two cavities in the unliganded state, 8.1 and 7.5 Å, respectively, these results suggest that large structural rearrangements occur during cavity transition from the long, narrow channel in the unliganded form to the final CD4 binding cavity in the liganded form upon CD4 binding.

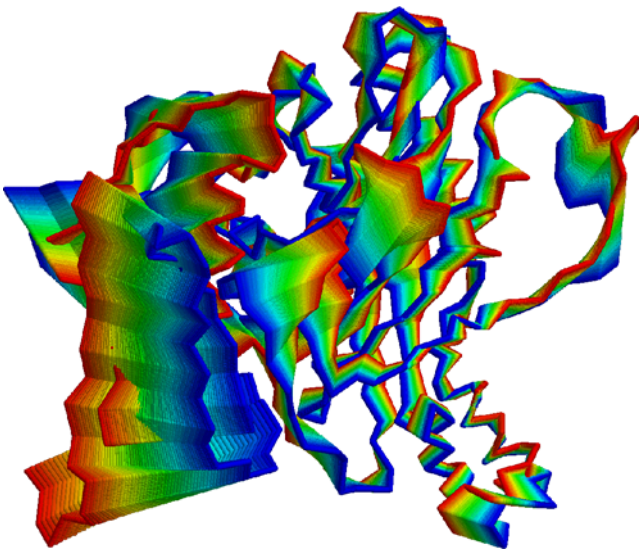

Fig. 4 Overlapping diagram of the liganded gp120 model against the unliganded one with linear frames interpolating between them. The interpolated frames are *colored from red* (unliganded) *to blue* (liganded) to highlight the primary structural differences between the two states but do not represent the transition pathway

Discussion

The prerequisite of our analysis of the gp120 dynamic domain is to obtain in depth knowledge of structures in both the liganded and unliganded states. The 100% sequence identity between the target sequence of the HXBc2 and its template 1G9M results in an accurate core structure of the liganded gp120 with approximately accurate V3 and V4 loop being modeled on this core as more than 98% residues in this model are located in the favored regions of the Ramachandran plot obtained from the PROCHECK program [38]. The direct experimental data of the unliganded structure of the HIV-1 gp120 is not available at this state, however, given the high sequence similarity (35% sequence identity and over 70% sequence similarity) between SIV and HIV, the unliganded HIV-1 gp120 is likely to assume a similar conformation because it was noted [30] that it is possible to generate medium-accuracy unliganded HIV-1 gp120 models where ~90% of the main-chain atoms can be modeled with 1.5 Å RMS error under such a sequence similarity. In our unliganded HIV-1 gp120 model with modeled V3 loop, there are more than 90% residues that have appropriate dihedral angle distributions. Furthermore, the relatively high overall sequence conservation between SIV and HIV, their common

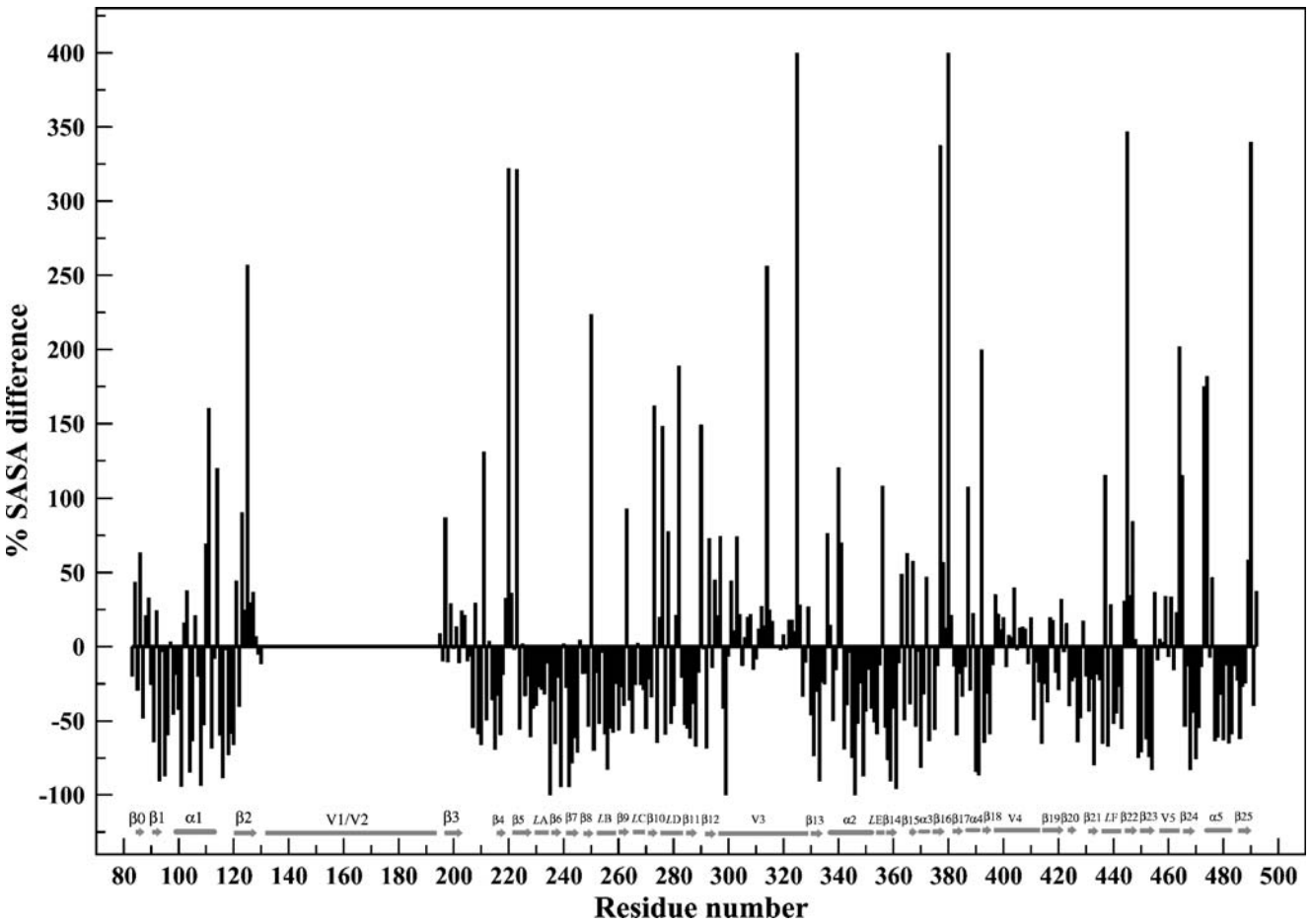

Fig. 5 Percentage of difference (%D_{SASA}) of the unliganded gp120 total solvent accessible surface area (SASA) per residue from the liganded gp120. The percentage is calculated from %D_{SASA}=($SASA_{liganded}$/$SASA_{unliganded}$−1)×100. If the SASA of the liganded state is smaller than that of the unliganded one, the %D_{SASA} is negative, otherwise it is positive. All atoms are taken into account for the calculations of SASA except for the V1/V2 loop. The secondary structure elements and loops are marked according to the liganded gp120

receptor and coreceptors, and as described in the literature [18], the crystal structure of the SIV gp120 is thus a good representation of the conformation in the CD4-unliganded state. Therefore most of differences between our HIV-1 homology models of the unliganded and liganded gp120s should reflect the conformational changes induced by receptor binding.

The dynamic domain analyses based on the two models reveal complex domain motions with variable combinations of the domain pairs. The results are not in line with

Table 4 Geometrical properties of the long, narrow cavity and CD4-binding cavity within the unliganded and liganded gp120 models

	RMSD[e] (Å)	NHB[f]	SASA[g] (Å^2)	NNC[h]	Rg[i] (Å)
Unliganded narrow cavity[a]	0.0	17.0	58.9	20,884.0	1.36
Unliganded CD4 cavity[b]	0.0	7.0	46.7	11,794.0	1.30
Liganded narrow cavity[c]	8.1	31.0	50.4	23,128.0	1.29
Liganded CD4 cavity[d]	7.5	4.0	47.2	11,648.0	1.42

[a] Geometrical properties of the long, narrow cavity within the unliganded state
[b] Geometrical properties of the CD4-binding cavity within the unliganded state
[c] Geometrical properties of the long, narrow cavity within the liganded state
[d] Geometrical properties of the CD4-binding cavity within the liganded state
[e] Backbone RMSD with respect to respective cavities within the unliganded state
[f] Number of hydrogen bonds
[g] Total solvent accessible surface
[h] Number of native contacts
[i] Radius of gyration

conventional domain delimitation, i.e. the entire gp120 cores are divided into the inner and outer domains according to their structural organization. On the contrary, both of the combined parameters for the DYNDOM obtained four definite domains, three of them arise from the inner domain and one of them from the outer domain. The intricately paired domain motion amongst the four subdomains indicates that the process of gp120-ligand association is not in agreement with the canonical domain motion observed in the bacteriophage T4 lysozyme [39] and *Streptococcus agalactiae* hyaluronate lyase [40], where the two enzymes were clustered into two domains, respectively, and one domain behaved as a closure or rotation/twisting motion relative to the other domain that was potentially related to the mechanism of the enzyme-substrate association. For the gp120 models, the α5 segment can be assigned either to the α1–β20–β21 domain or to the bending residue region connecting the N-, C-terminal domain and the outer domain; some of the screw axes are not the effective hinge axes while the others are; a majority of the domain pairs show mixed motional modes of the closure, twisting, and translation with respect to each other and have long, flexible bending residue regions. All of these results reveal that the intricate dynamics of conformational changes at the domain level is accompanied by receptor association.

Dynamic domain analyses also reveal that the V1/V2 stem (β2–β3 ribbon) of the partial bridging sheet, in particular, experiences the largest magnitudes of rotation and translation among the four paired domains (Table 1 and Table 2), while the domains containing the β20–β21, another half the bridging sheet, either are the fixed domains or move moderately compared to the V1/V2 stem, indicating that the V1/V2 stem is the most mobile domain in the gp120, and these results are in agreement with the MD simulation data [41, 42]. We speculate the high flexibility of the V1/V2 stem may make its conformation change dramatically in both the unliganded and liganded states, and some of the populated conformers near the unliganded conformation can serve as intermediates that might be the starting conformations that favor more efficient CD4 recognition/association under the physiological condition.

The geometrical property analyses of the cavities reveal that the long, narrow cavity in the unliganded state has more SASA and NNC while smaller Rg than the CD4-binding cavity in the liganded state, indicating the CD4's association is not simply a wedging process. The large SASA of the long, narrow cavity in the unliganded state is advantageous for forming large contact surface for the CD4 molecule. However, we speculate that the initial contact of CD4 with gp120 might induce residues within the narrow cavity to reposition their orientations that further result in decreases of the SASA and NNC, and then, the non-bond (static electricity and van der Waals) and hydrogen-bond interactions will drive the CD4 to insert into its binding pocket [43], such insertion makes the gp120 continually reconfigure its conformation to enlarge the CD4 binding pocket, and finally, this pocket translates into the ultimate CD4 binding cavity with a larger Rg as observed in the liganded gp120. It is worth pointing out that the initial contact sites for the CD4 or other ligands (such as CD4BS antibodies or small molecule inhibitors) are located at the structural components (α1, α5, CD4-BL, β20–β21 ribbon) constituting the long, narrow channel in the unliganded gp120 [18, 19], whereas the complexation with ligands results in conformational changes that make this channel transition to different conformational forms, which possess the distinct ligand contact sites from the original narrow channel. Another interesting finding is that the CD4's association reduces contents of the coil and bend while increase contents of the α-helix and β-sheet, which is in agreement with the circular dichroism study on the gp120-CD4 complex formation [20]. It should be noted that we did not simulate the binding process and therefore no kinetic or free energy data could be obtained from the current study, the structural property analyses of the unliganded and liganded states and of the two cavities within both of the states merely presents a geometrical view that can be used to extract certain valuable information and speculate possible cavity transition mode of the gp120 upon the receptor binding.

Thermodynamic studies of the monomeric gp120 indicate that the gp120-CD4 complex formation is accompanied by an unusually large entropic loss, which is compensated by a gain in enthalpy through the intermolecular interactions [19, 20]. Antibodies that recognize the CD4-binding (CD4BS) and CD4-induced (CD4i) sites also have the large negative binding entropy and correspondingly large negative enthalpy [20]. This entropy cost reduces antibody and receptor affinity and provides one probable explanation for the failure of the gp120 to induce potent neutralizing antibodies against the CD4BS and CD4i sites [19]. Empirical relationships between the thermodynamic parameters and conformational differences suggest that the measured entropy and enthalpy changes could infer either the burial of 10,000 (±2,000 $Å^2$) of molecular surface or the ordering of about 94 (±15) residues [20]. SASA calculations (Table 3) based on the unliganded and liganded gp120 models show that about 4,065 $Å^2$ is sequestered from the solvent, plus the buried area of 1,544 $Å^2$ at the gp120-CD4 interfaces, a total 5,609 $Å^2$ in area is buried when the CD4 and gp120 associate. Secondary structure element statistics (Table 3) of the two conformational states reveals that about 82 residues acquire ordered conformations. The structural properties analyses from our models are in reasonable agreement with thermodynamic studies and empirical prediction.

In a recent study, Hsu and Bonvin [43] performed 10 ns MD simulations on the liganded gp120 (CD4-free gp120 in the CD4-bound state) and gp120-CD4 complex to investigate the conformational changes of gp120 upon CD4 complexation. By comparison the dynamics property of the CD4-free gp120 with that of the complex form, they found that CD4's association reduced conformational flexibility for some loop regions of the outer domain, and this process accompanied an extensive hydrogen bond formation between the CD4 and CD4 binding cavity. Therefore, a "binding funnel" model was proposed to explain the CD4's association mechanism. Although valuable information was obtained from their MD simulations, the lack of the unliganded gp120 structure leads to the underestimations of the conformational flexibility in the ordered regions as well as the extent of conformational rearrangements upon CD4 association. Our analysis in this paper compensates the MD studies, for instance, the structural overlap shown in Fig. 4 indicates that large conformational changes occurred not only in the loops of the outer domain, but also in the ordered structural components of both the inner and outer domains. Based on the geometrical analyses and cavity transition mode as well as the thermodynamic [19, 20] and MD [43] studies described above, we speculate that the gp120-CD4's association should be a process of "induced fit": first, the long range electrostatic interactions between charged residues in highly flexible structural components of the unliganded gp120 and CD4 drive them to approach mutually; second, the approach of the CD4 to gp120 induces structural components of the long, narrow channel to reorganize their positions to form more contacting sites for the CD4; third, the gradually increasing hydrogen-bond and hydrophobic interactions drive the CD4 to wedge into the narrow cavity; and finally, the gp120 sequentially adjusts its conformation to accommodate CD4's wedging until the final CD4 cavity forms and the phenyl ring of the Phe43 fits into its binding pocket. The natural unliganded gp120 is constantly subject to the immune system attack in vivo and a definite CD4 binding pocket would be an ideal target for antibodies neutralization, therefore the gp120 carries out the combined strategies of loop masking and conformational flexibility on the CD4- and chemokine-receptor-binding sites to escape from immune system surveillance, and devises a multi-level induced fit mechanism to facilitate the CD4 binding.

It is not clear whether the bridging sheet has been formed after CD4's association while prior to coreceptor or 17b Fab's binding. However, our dynamic domain analyses show that the gp120 inner domain is clustered into three separate subdomains (N-, C-terminal, V1/V2 stem, and α1–β20–β21 domains) that involve in independent domain motions, implying that the V1/V2 stem may not be fully docked against the β20–β21 ribbon. The V1/V2 stem's high mobility revealed by the dynamic domain analyses suggests that the V1/V2 stem might first lose its contact with the inner domain in the unliganded gp120 to leave space for movements of the α1 and β20–β21 towards the liganded form upon CD4 binding, and furthermore, the MD data [41, 42] indicate that the CD4's association just partially locks the bridging sheet and still leaves the V1/V2 stem flexible, we speculate that the following binding of coreceptor would continue pulling the halves of the bridging sheet into close proximity to stabilize the CD4-bound state and lock the bridging-sheet.

The conformation of the gp120 is constrained in its assembly with the gp41 into a trimeric complex on the virion surface [3–5], and the ability of many conformationally sensitive monoclonal antibodies to neutralize HIV-1 has been associated with their affinity for the trimeric envelope virion structure [44]. The models of the liganded and unliganded gp120 trimers have been created by Kwong et al. [45] and Chen et al. [18], respectively. In these models, the N-, C-termini of the gp120 pointed towards the gp41 and centered on the three-fold axis, the carbohydrates were maximum exposed, and the contacts between the V1/V2 in one unit and the V3 in another unit could be observed. Interestingly, the motional features obtained from our dynamic domain analyses of the monomeric gp120 resemble those observed for the unliganded trimer. In the unliganded gp120 trimer, the N-, C-termini and the three-stranded β-bundle of the inner domain interact with the gp41, therefore they are relatively immobilized while all the other structural components of the gp120 can move with respect to them. Analogously, Fig. 3 shows that the N-, C-terminal (including β5–β7–β25) domain is fixed, whereas the moving domains such as the V1/V2 stem, outer domain, and α1–β20–β21 can rotate/translate around/along the corresponding axes relative to the fixed N-, C-terminal domain, causing formation of the coreceptor site that faces away from the direction of the N-, C-termini and towards the target cell. The hinge bending residues 204–214 between the V1/V2 stem and N-, C-termini possess the highly conformational flexibility, which is stretched into an extended strand and such a displacement might contribute to the dissociation of the gp120 from the gp41, releasing the latter to commit to the fusion transition.

To summarize, our homology models of the unliganded and liganded HIV-1 gp120 represent two distinct conformational states, namely the looser, flexible, and disordered ground state and the compact, rigid, and ordered excited state, respectively. Dynamic domain studies reveal that intricately motional modes occur between domain pairs combined respectively from four distinct clustered domains, and the domain motions are in line with those described in the trimer model. Geometrical property calculations and

structure overlap of the two models indicate that not only the variable loops, but also the ordered structural components in gp120 undergo large conformational rearrangements. The total molecular surface burial and ordering residue quantity from our calculations are in agreement with empirical deduction from thermodynamic studies. The highly conformational flexibility and the inferred cavity transition mode based on the geometrical analysis, in combination with different interaction modes between CD4 and gp120 as described by Hsu and Bonvin [43] allow us to propose an induced fit model to explain the molecular recognition-binding mechanism that compensates the crystallographic and MD studies. Furthermore, the target MD simulation or umbrella sampling should be performed to explore the possibilities of the physically accessible transition pathways between the unliganded and liganded gp120.

Acknowledgements The authors thank Sara Barton for careful reading and helpful comments, and High Performance Computer Center of Yunnan University for computational support. This work was supported by grants from the Yunnan University (2004Q013B), Yunnan Province (2006C0008M), open fund from Laboratory for Conservation and Utilization of Bio-resources, Yunnan University, and Innovation Group Project from Yunnan University.

References

1. Barre-Sinoussi F, Chermann JC, Rey F, Nugeyre MT, Chamaret S, Gruest J, Dauguet C, Axler-Blin C, Vezinet-Brun F, Rouzioux C, Rozenbaum W, Montagnier L (1983) Science 220:868–871
2. Gallo RC, Salahuddin SZ, Popovic M, Shearer GM, Kaplan M, Haynes BF, Palker TJ, Redfield R, Oleske J, Safai B (1984) Science 224:500–503
3. Allan JS, Coligan JE, Barin F, McLane MF, Sodroski JG, Rosen CA, Haseltine WA, Lee TH, Essex M (1985) Science 228:1091–1094
4. Veronese FD, DeVico AL, Copeland TD, Oroszlan S, Gallo RC, Sarngadharan MG (1985) Science 229:1402–1405
5. Center RJ, Leapman RD, Lebowitz J, Arthur LO, Earl PL, Moss B (2002) J Virol 76:7863–7867
6. Dalgleish AG, Beverley PC, Clapham PR, Crawford DH, Greaves MF, Weiss RA (1984) Nature 312:763–767
7. Feng Y, Broder CC, Kennedy PE, Berger EA (1996) Science 272:872–877
8. Trkola A, Dragic T, Arthos J, Binley JM, Olson WC, Allaway GP, Cheng-Mayer C, Robinson J, Maddon PJ, Moore JP (1996) Nature 384:184–187
9. Wu L, Gerard NP, Wyatt R, Choe H, Parolin C, Ruffing N, Borsetti A, Cardoso AA, Desjardin E, Newman W, Gerard C, Sodroski J (1996) Nature 384:179–183
10. Rizzuto CD, Wyatt R, Hernandez-Ramos N, Sun Y, Kwong PD, Hendrickson WA, Sodroski J (1998) Science 280:1949–1953
11. Liu SQ, Fan SX, Sun ZR (2003) J Mol Mod 9:329–336
12. Liu SQ, Shi XF, Liu CQ, Sun ZR (2004) J Mol Struct (THEOCHEM) 673:133–143
13. Chan DC, Fass D, Berger JM, Kim PS (1997) Cell 89:263–273
14. Weissenhorn W, Dessen A, Harrison SC, Skehel JJ, Wiley DC (1997) Nature 387:426–430
15. Kwong PD, Wyatt R, Robinson J, Sweet RW, Sodroski J, Hendrickson WA (1998) Nature 393:648–659
16. Kwong PD, Wyatt R, Majeed S, Robinson J, Sweet RW, Sodroski J, Hendrickson WA (2000) Structure Fold Des 8:1329–1339
17. Wyatt R, Kwong PD, Desjardins E, Sweet RW, Robinson J, Hendrickson WA (1998) Nature 393:705–711
18. Chen B, Vogan EM, Gong H, Skehel JJ, Wiley DC, Harrison SC (2005) Nature 433:834–841
19. Kwong PD, Doyle ML, Casper DJ, Cicala C, Leavitt SA, Majeed S, Steenbeke TD, Venturi M, Chaiken I, Fung M, Katinger H, Parren PW, Robinson J, Van Ryk D, Wang L, Burton DR, Freire E, Wyatt R, Sodroski J, Hendrickson WA, Arthos J (2002) Nature 420:678–682
20. Myszka DG, Sweet RW, Hensley P, Brigham-Burke M, Kwong PD, Hendrickson WA, Wyatt R, Sodroski J, Doyle ML (2000) Proc Natl Acad Sci USA 97:9026–9031
21. Rusche JR, Javaherian K, McDanal C, Petro J, Lynn DL, Grimaila R, Langlois A, Gallo RC, Arthur LO, Fischinger PJ, Bolognesi DP, Putney SD, Matthews TJ (1988) Proc Natl Acad Sci USA 85:3198–3202
22. Berger EA, Murphy PM, Farber JM (1999) Annu Rev Immunol 17:657–700
23. Rini JM, Stanfield RL, Stura EA, Salinas PA, Profy AT, Wilson IA (1993) Proc Natl Acad Sci USA 90:6325–6329
24. Tugarinov V, Zvi A, Levy R, Hayek Y, Matsushita S, Anglister J (2000) Struct Fold Des 8:385–395
25. Sharon M, Kessler N, Levy R, Zolla-Pazner S, Gorlach M, Anglister J (2003) Structure 11:225–236
26. Huang CC, Tang M, Zhang MY, Majeed S, Montabana E, Stanfield RL, Dimitrov DS, Korber B, Sodroski J, Wilson IA, Wyatt R, Kwong PD (2005) Science 310:1025–1028
27. Bairoch A, Apweiler R, Wu CH, Barker WC, Boeckmann B, Ferro S, Gasteiger E, Huang H, Lopez R, Magrane M, Martin MJ, Natale DA, O'Donovan C, Redaschi N, Yeh, LS (2005) Nucl Acids Res 33 (Database issue):D154–159
28. Deshpande N, Addess KJ, Bluhm WF, Merino-Ott JC, Townsend-Merino W, Zhang Q (2005) Nucl Acids Res 33 (Database issue): D233–237
29. Vranken WF, Budesinsky M, Fant F, Boulez K, Borremans FA (1995) FEBS Lett 374:117–121
30. Baker D, Sali A (2001) Science 294:93–96
31. Humphrey W, Dalke A, Schulten K (1996) J Mol Graph 14(33–38):27–28
32. Sali A, Blundell TL (1993) J Mol Biol 234:779–815
33. Hayward S, Kitao A, Berendsen HJ (1997) Proteins 27:425–437
34. Hayward S, Berendsen HJ (1998) Proteins 30:144–154
35. Van Der Spoel D, Lindahl E, Hess B, Groenhof G, Mark AE, Berendsen HJ (2005) J Comput Chem 26:1701–1718
36. Lindahl E, Hess B, Van Der Spoel D (2001) J Mol Mod 7:306–317
37. Kabsch W, Sander C (1983) Biopolymers 22:2577–2637
38. Laskowski RA, MacArthur M, Moss DS, Thornton JM (1993) J Appl Crystallogr 26:283–291
39. de Groot BL, Hayward S, Van Aalten DM, Amadei A, Berendsen HJ (1998) Proteins 31:116–127
40. Mello LV, De Groot BL, Li S, Jedrzejas MJ (2002) J Biol Chem 277:36678–36688
41. Pan Y, Ma B, Keskin O, Nussinov R (2004) J Biol Chem 279:30523–30530
42. Pan Y, Ma B, Nussinov R (2005) J Mol Biol 350:514–527
43. Hsu ST, Bonvin AM (2004) Proteins 55:582–593
44. Poignard P, Saphire EO, Parren P, Burton, DR (2001) Annu Rev Immunol 19:253–274
45. Kwong PD, Wyatt R, Sattentau QJ, Sodroski J, Hendrickson WA (2000) J Virol 74:1961–1972
46. Ramachandran GN, Ramakrishnan C, Sasisekharan V (1963) J Mol Biol 7:95–99
47. Kraulis PJ (1991) J Appl Cryst 24:946–950
48. Sayle RA, Milner-White EJ (1995) Trends Biochem Sci 20:374–376